FULL PAPER

ADVANCED
ENERGY
MATERIALS

Printed Supercapacitors

www.advenergymat.de

Versatile N-Doped MXene Ink for Printed Electrochemical Energy Storage Application

Lianghao Yu, Zhaodi Fan, Yuanlong Shao,* Zhengnan Tian, Jingyu Sun,* and Zhongfan Liu

Printing is regarded as a revolutionary and feasible technique to guide the fabrication of versatile functional systems with designed architectures. 2D MXenes are nowadays attractive in printed energy storage devices. However, owing to the van der Waals interaction between the MXene layers, the restacking issues within the printed electrodes can significantly impede the ion/electrolyte transport and hence handicap the electrochemical performances. Herein, a melamine formaldehyde templating method is demonstrated to develop crumpled nitrogen-doped MXene (MXene-N) nanosheets. The nitrogen doping boosts the electrochemical performances of MXene via enhanced conductivity and redox activity. Accordingly, two types of MXene-N inks are prepared throughout the optimization of the ink viscosity to fit the 2D screen printing and 3D extrusion printing, respectively. As a result, the screen printed MXene-N microsupercapacitor delivers an areal capacitance of 70.1 mF cm^{-2} and outstanding mechanical robustness. Furthermore, the 3D-printed MXene-N based supercapacitor manifests an areal capacitance of 8.2 F cm^{-2} for a three-layered electrode and readily stores a high areal energy density of 0.42 mWh cm^{-2}. The approach to harnessing such versatile MXene-N inks offers distinctive insights into the printed energy storage systems with high areal energy density and large scalability.

1. Introduction

The emergence of smart, wearable electronic systems has stimulated the development of next-generation flexible energy storage devices with matchable size in different dimensions.[1–3] Amid them, supercapacitor (SC) has been regarded as a promising power source that can offer high power density, long lifespan, and low cost.[4–7] To date, substantial progress has been made in developing the construction methodologies of SCs, encompassing blade spreading, dip coating, laser scribing, mask-assisted filtration, etc.[8–10] Nevertheless, these techniques still suffer from intrinsic drawbacks such as low efficiency, limited material utilization, and tedious manufacturing steps, thereby impeding large-scale and low-cost device fabrication in an accurate and effective fashion.

Recent years have witnessed a growing interest in the employment of direct printing techniques (e.g., screen printing and extrusion printing)[1,11] in building up wearable energy storage device, which are versatile enough to design desirable patterning and enable geometric flexibility. Screen printing holds widespread prospects for deriving flexible and planar electrodes for micro-SC (MSC) in a facile and scalable manner, whilst extrusion-based 3D printing is in high demand to allow rapid digital processing for customized SC patterning.[12,13] In this sense, the rheological properties of the used inks would be key to enable different printing protocols. For instance, more viscous ink is needed for extrusion printing as compared to screen printing, which is sustainable to hold printed 3D architectures without collapse. As for the materialwise consideration for functional inks, many efforts have been devoted to the selection of transition metal oxides (e.g., MnO_2,[14] V_2O_5,[15] and Co_3O_4[16]) with pseudocapacitive features. However, their poor conductivity would jeopardize the power density of thus-derived SC. Moreover, while ubiquitous carbon-based electrode materials such as graphene,[17] activated carbon (AC),[18] and carbon nanotubes (CNTs)[19] are promising to store charge throughout the formation of electrochemical double layer capacitance, their low tap density (graphene: ≈0.4 g cm^{-3})[20] and insufficient areal energy density otherwise limit the practical applications especially in compact energy storage realms.

L. H. Yu, Z. D. Fan, Z. N. Tian, Prof. J. Y. Sun, Prof. Z. F. Liu
College of Energy
Soochow Institute for Energy and Materials Innovations (SIEMIS)
Key Laboratory of Advanced Carbon Materials and Wearable Energy Technologies of Jiangsu Province
Soochow University
Suzhou 215006, P. R. China
E-mail: sunjy86@suda.edu.cn
Dr. Y. L. Shao
Physical Sciences and Engineering Division
King Abdullah University of Science and Technology
Thuwal 23955-6900, Saudi Arabia
E-mail: yuanlong.shao@kaust.edu.sa, yuanlong.shao@gmail.com
Prof. Z. F. Liu
Center for Nanochemistry (CNC)
Beijing Science and Engineering Center for Nanocarbons
College of Chemistry and Molecular Engineering
Peking University
Beijing 100871, P. R. China

MXene (Ti_3C_2), a fascinating 2D transition metal carbide possessing excellent electrical conductivity ($\approx 10^4$ S cm^{-1}), favorable hydrophilicity, high tap density (4.0 g cm^{-3}), and large capacitance (up to 1500 F cm^{-3}) has been regarded as a promising electrode candidate for metal-ion batteries and SC.[20,21] Unfortunately, similar to other 2D congeners such as graphene and MoS$_2$,[22] the van der Waals force induced sheet-to-sheet restacking normally limits the ion/electrolyte transport within electrodes, thereby handicapping the electrochemical performance of MXene. In response, template-guided synthesis of porous MXene nanosheets has recently emerged as a feasible solution to tackle the obstacle for aggregation, benefiting from the mutual interaction between positively charged templating agents and negatively charged MXene flakes (with −F, −O, and −OH terminal groups).[23,24] Gogotsi and co-workers demonstrated the use of polymethyl methacrylate sphere templates to prepare 3D macroporous MXene frameworks for application in sodium-ion battery.[25] Nevertheless, investigations on the employment of well-dispersed MXene nanosheets to construct printable SC devices targeting high areal and volumetric capacitances are still in an infancy.

In the present work, we demonstrate the direct printing of crumpled nitrogen-doped MXene (MXene-N) nanosheets for the construction of wearable symmetric SCs with landmark areal and volumetric energy densities. Our crumpled MXene-N synergizing versatile pore structure and uniform N-doping can be simply obtained by applying a melamine formaldehyde (MF) template method. The heteroatom nitrogen doping is beneficial to augmenting the conductivity and enhancing the electrochemical reactivity throughout surface modification. Accordingly, two types of MXene-N inks, namely binder-additive aqueous ink and binder-free hybrid ink, are explored for screen printing and extrusion printing, respectively. As a result, the flexible all-MXene-N printed MSCs via screen printing delivers a high areal capacitance of 70.1 mF cm^{-2}, outperforming the state-of-the-art MXene-based MSCs reported by far. In addition, the 3D extrusion printing process enables the fabrication of

thick electrodes by controlled layer-by-layer deposition, readily harvesting a high areal energy density of 0.42 mWh cm^{-2}. Our work demonstrates that the direct printing of emerging MXene materials offers great potential for scalable and customizable manufacturing of high-energy electrodes for wearable energy storage devices.

2. Results and Discussion

Figure 1 schematically illustrates the direct printing process of MXene-N ink toward the construction of symmetric SC devices. The key material for the ink formulation, crumpled MXene-N nanosheets, was fabricated by an MF templating method. It starts with the employment of few-layer MXene flakes as the precursor, which were exfoliated throughout a wet etching (HCl + LiF) procedure (Figures S1 and S2, Supporting Information). Atomic force microscopy analysis confirms ultrathin nature (with a survey thickness of 3.15 nm) of the exfoliated MXene nanosheets. A conspicuous Tyndall effect can also be observed for the aqueous suspension of MXene flakes, indicative of their colloidal structure (Figure S3, Supporting Information).[26] Upon the addition of MF template into such MXene suspension, these flakes spontaneously wrap the surface of MF spheres because of the electrostatic interaction between their surface functional groups (Figure S4, Supporting Information).[23] This is followed by annealing in Ar ambient at 550 °C for 2 h to remove MF template and finally, to produce crumpled MXene-N nanosheets. The involvement of MF templates not only prevents MXene nanosheets from restacking but also affords nitrogen doping into MXene frameworks. With thus-prepared MXene-N nanosheets in hand, two types of inks can be readily formulated to fit for different printing uses. A binder-additive aqueous ink can be designed to screen print planar MSCs. On the other hand, a binder-free composite ink is formed by adding graphene oxide (GO) solution to tune the viscosity, leading to the extrusion printing of MXene-N based
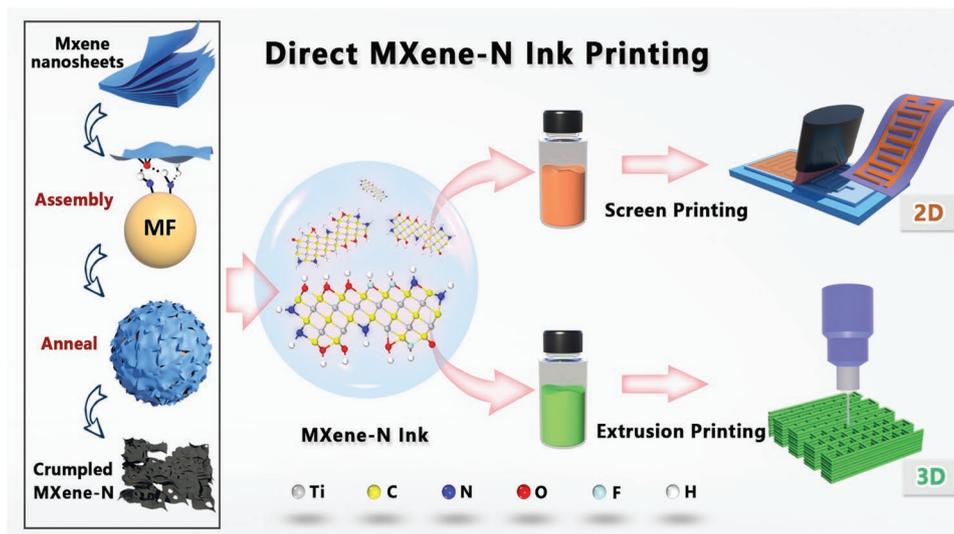
Figure 1. Schematic illustration of direct MXene-N ink printing. Left panel: Synthesis of crumpled MXene-N. Right panel: Versatile MXene-N inks designed for printing, namely, screen printing of 2D pattern (top row) and extrusion printing of 3D architecture (bottom row).
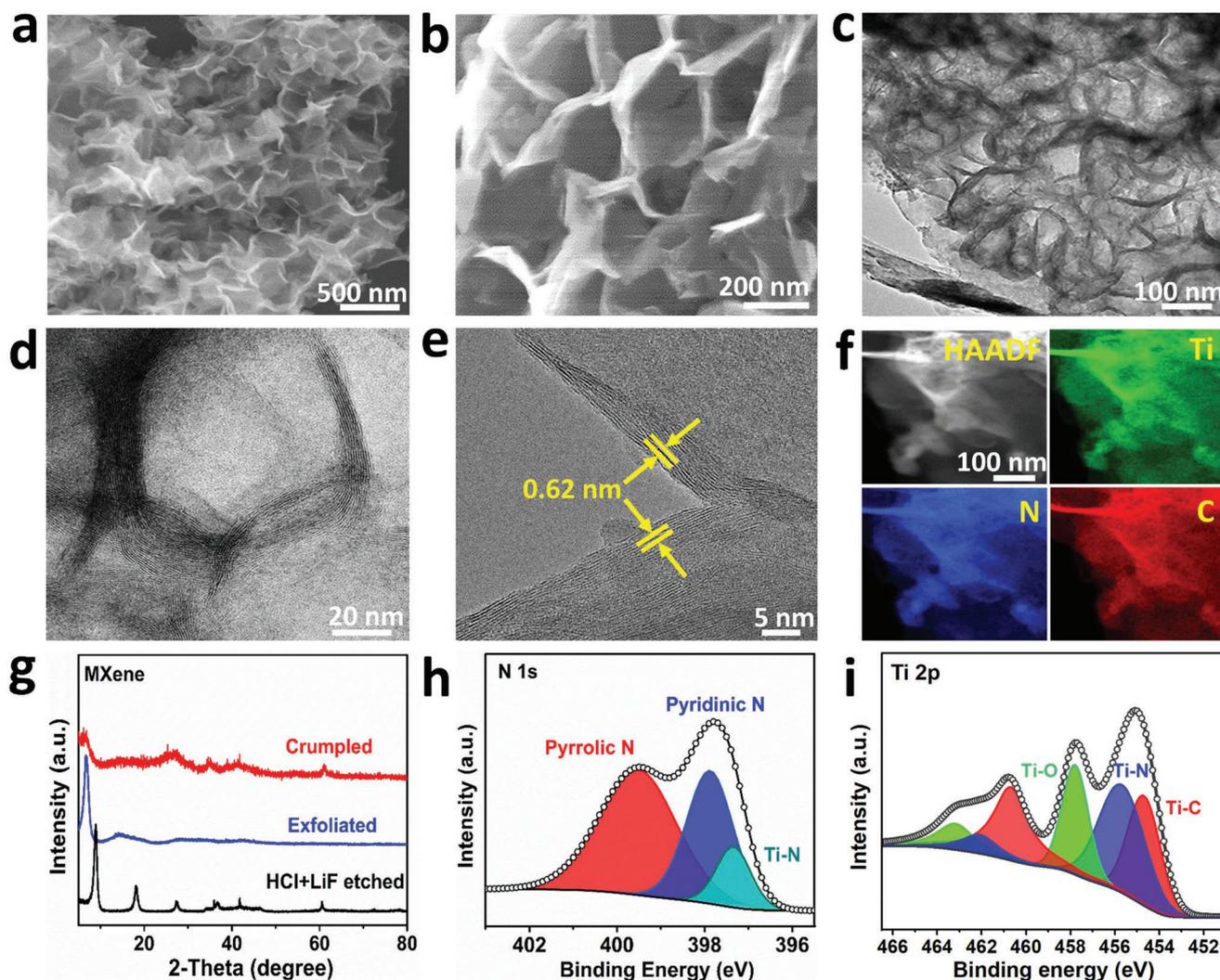
Figure 2. a,b) SEM images of crumpled MXene-N nanosheets. c,d) TEM images of crumpled MXene-N nanosheets. e) HRTEM image showing the interlayer distance between two neighboring MXene-N layers. f) Scanning transmission electron microscopy image and elemental maps of MXene-N. g) XRD of the etched, exfoliated, and crumpled MXene. h,i) N 1s and Ti 2p XPS spectrum of crumpled MXene-N nanosheets, respectively.

3D SC devices. The direct printing of versatile MXene-N inks with different dimensions is of great significance for building up wearable energy device arrays in a scalable manner.

The resulting MXene-N products were subject to a wide suite of characterization techniques, as revealed in **Figure 2**. The morphology was mainly characterized by scanning electron microscopy (SEM) and transmission electron microscopy (TEM). The SEM images in Figure 2a,b display porous networks of MXene-N with ample porosity, which are assembled from numerous MXene flakes guided by MF templates. Low-magnified TEM observation in Figure 2c further exhibits the detailed structure of crumpled MXene-N. The successful template-dictated formation of ultrathin $Ti_3C_2T_x$ shells is also confirmed by enlarged TEM views (Figure 2d and Figure S5, Supporting Information), synergistically restraining the restacking of delaminated MXene nanosheets and incorporating foreign nitrogen dopants. High-resolution TEM (HRTEM) image (Figure 2e) clearly manifests lattice fringes with an interlayer spacing of ≈0.62 nm, agreeing well with the previous

reports.[27] In addition, the high-angle annular dark field image and corresponding elemental mappings (Figure 2f) show an even distribution of the Ti, C, and N elements in the probed area, indicative of the uniform nitrogen doping within the sample. To further elucidate the phase information and chemical compositions of synthesized MXene-N, X-ray diffraction (XRD), and X-ray photoelectron spectroscopy (XPS) analysis were carried out. XRD patterns in Figure 2g manifest that the etched MXene displays an intense (002) peak at 8.95°, whereas the (002) peak pertaining to the exfoliated MXene and crumpled MXene-N centers at 6.68° and 6.13°, respectively. Such observable peak downshifts suggest increased interlayer distance of MXene, which might stem from the condensation of water molecules and the incorporation of N heteroatoms on the MXene skeleton.[28]

Moreover, the N doping is also beneficial to augmenting the electrical conductivity and enhancing the electrochemical property throughout surface modification.[29] XPS survey spectra of etched MXene and crumpled MXene-N samples further

ADVANCED
SCIENCE NEWS
www.advancedsciencenews.com

ADVANCED
ENERGY
MATERIALS
www.advenergymat.de
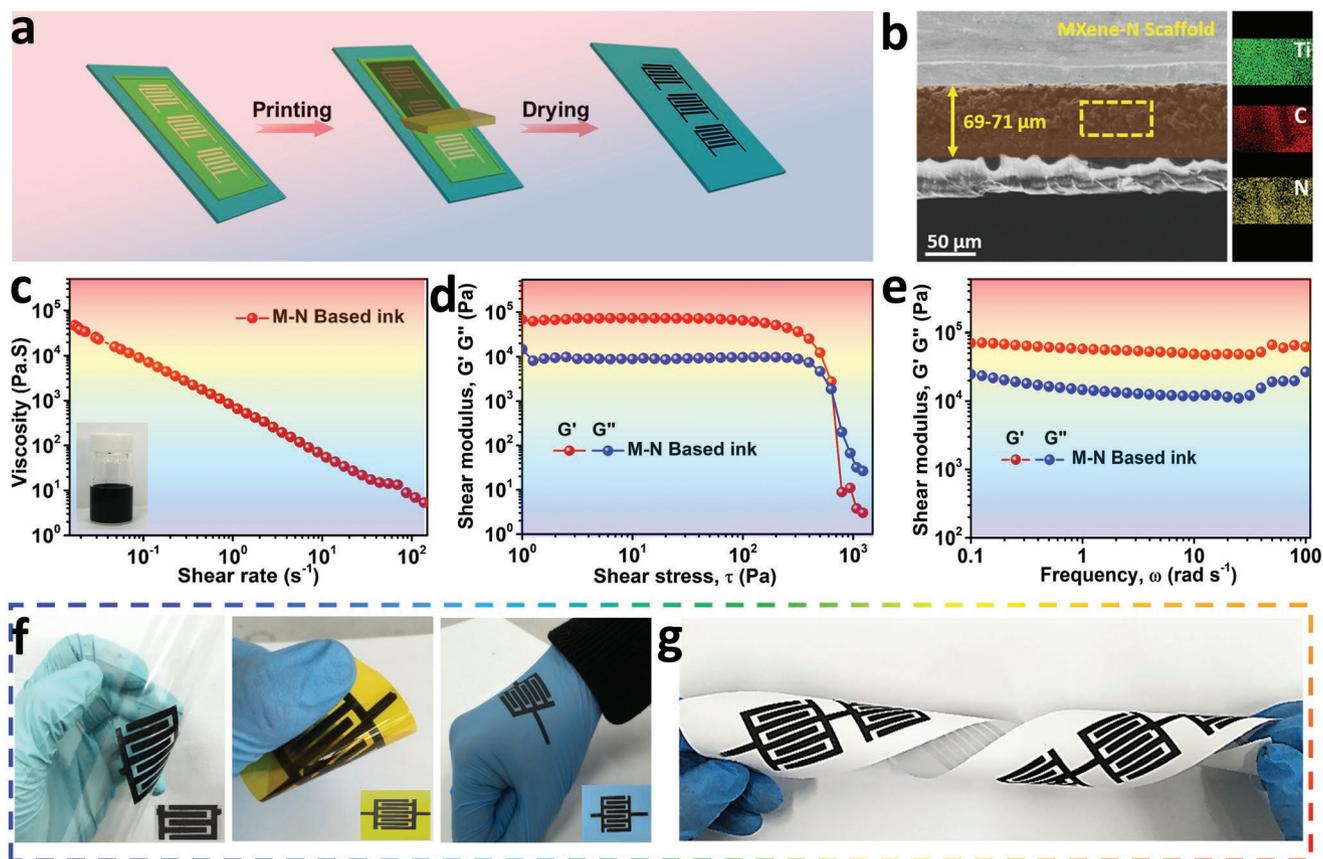
Figure 3. a) Schematic illustration showing the fabrication process of MXene-N MSCs via screen printing. b) Cross-sectional SEM image of the printed electrode and corresponding elemental maps of Ti, C, and N. c) Apparent viscosity of as-fabricated MXene-N ink as a function of shear rate. d,e) The storage modulus (G') and loss modulus (G'') of MXene-N ink as functions of d) shear stress and e) angle frequency. f) Digital photographs of all-MXene-N printed MSC on various substrates at bent and flat states. g) Photo showing the flexibility of MSC devices connected in series.

corroborate the successful nitrogen doping (Figure S6, Supporting Information). A recent study by Bao et al. reported that as-synthesized nitrogen-doped $Ti_3C_2T_x$ nanosheets demonstrated three peaks at 397, 398.3, and 399.8 eV at the XPS N 1s spectrum, corresponding to Ti–N, pyridinic N, and pyrrolic N.[23] In our case, Figure 2h shows XPS N 1s spectrum of crumpled MXene-N. The deconvoluted peaks at 397.3 ± 0.1, 397.8 ± 0.1, and 399.8 ± 0.1 eV can be clearly observed, which can be accordingly assigned to Ti–N, pyridinic N, and pyrrolic N signal, respectively. The existence of C and N bonding can be further corroborated by high-resolution C 1s spectrum (Figure S7a, Supporting Information). The O 1s spectrum of MXene-N reveals the bonding information of N–O with a small content of 4.9% (Figure S7b, Supporting Information), indicating that the nitrogen dopants were partially incorporated into the surface functional groups during sample preparation. XPS Ti 2p spectrum in Figure 2i also displays three conspicuous peaks at 454.7, 455.7, and 457.8 eV, which can be assigned to the contribution from Ti–C, Ti–N, and Ti–O bonding, respectively.[23,30] The observation of Ti–N peak in both N 1s and Ti 2p spectra offers confirmation with respect to the substitution of C atoms in the MXene matrix by the N atoms. Moreover, it is noted that the crumpled MXene-N possesses a surface area of 234.1 m^2 g^{-1} and a pore volume of 0.256 cm^3 g^{-1}

as demonstrated by the N_2 adsorption/desorption isotherm (Figure S8, Supporting Information).

Figure 3a illustrates the fabrication procedure of MXene-N MSCs via screen printing. First, a designed mask was obtained by photochemigraphy method, followed by dropping off MXene-N slurry on the side of the screen. Upon applying a squeegee with a velocity of 2 cm s^{-1}, the paste can transfer from the mask to the substrate. Finally, a continuous MXene-N interdigital electrode was readily formed after a simple drying process. Cross-sectional SEM examination of the printed electrode clearly shows an interconnected scaffold without any structural collapse. In addition, C, N, and Ti elements were detected in homogeneous distributions by elemental mapping analysis (Figure 3b). To enable such a 2D screen printing process, a highly stable and conductive MXene-N ink was derived by mixing active materials, Super P, and LA132 binder in deionized water (Figure S9, Supporting Information). As shown in Figure 3c, the MXene-N ink exhibits a shear-thinning non-Newtonian fluid behavior, implying the viscosity decreasing with increasing shear rates, which is essential for printable ink to flow continuously. At an initial shear rate of 0.05 s^{-1}, the ink possesses high viscosities (>10^4 Pa s) to enable the printing with fine patterns, thereby preventing the entire device from short circuit. Figure 3d displays the storage

modulus (G′) and loss modulus (G″) of the ink. Under a low shear stress (<100 Pa), G′ value is an order of magnitude higher than that of G″, implying an elastic behavior.[15] With the increased shear stress (>500 Pa), G″ plays a dominating role, indicating that the ink is favorable to be extruded from the mask to the substrate. Figure 3e further shows the oscillatory frequency sweep results, where both G′ and G″ are frequency independence. Meanwhile, it can be observed that G′ is higher than G″ within the entire frequency range, suggesting the preparation of a quite stable ink.[17] Moreover, the effect of solvent amounts (e.g., from 1.7 to 2.8 g) on the rheological properties of ink was probed, as shown in Figure S10 in the Supporting Information. It is obvious that the high dosage of solvent (2.8 g) would result in a dominant liquid-like behavior, which is not suitable for screen printing.

As such, direct printing of MXene-N ink can be carried out on a myriad of functional substrates, including polyethylene terephthalate, polyimide (PI), rubber, A4 paper, and other substrates such as Al foil, Cu foil, glass, and stainless steel plate (Figure S11, Supporting Information). Under various bending states, the printed patterns were firmly attached to the substrate with no structure degradation or delamination (Figure 3f), showing favorable adhesion. With the aid of screen printing, 2D interdigital electrodes without metal current collector show favorable flexibility and can be built in series in a short time scale (Figure 3g). Furthermore, quasi-solid-state SC full cells can be constructed by applying a gel electrolyte of polyvinyl alcohol/H_2SO_4 onto the interdigital electrodes (Figure S12, Supporting Information). Optical microscopy observation indicates that these electrodes possess fine edges and smooth appearance (Figure S13, Supporting Information) benefiting from the well-controlled printing process.

Figure 4a schematically depicts the quasi-solid-state MSC devices directly printed onto flexible PI support, encompassing MXene-N interdigital electrodes arranged in a symmetrical manner. Cyclic voltammetry (CV) profiles at different scan rates (10–100 mV s^{-1}) manifest apparent pseudocapacitive feature of N-MXene (Figure 4b), in good agreement with reported work.[29] Galvanostatic charge/discharge (GCD) curves of printed MSCs show triangular-like shapes under various
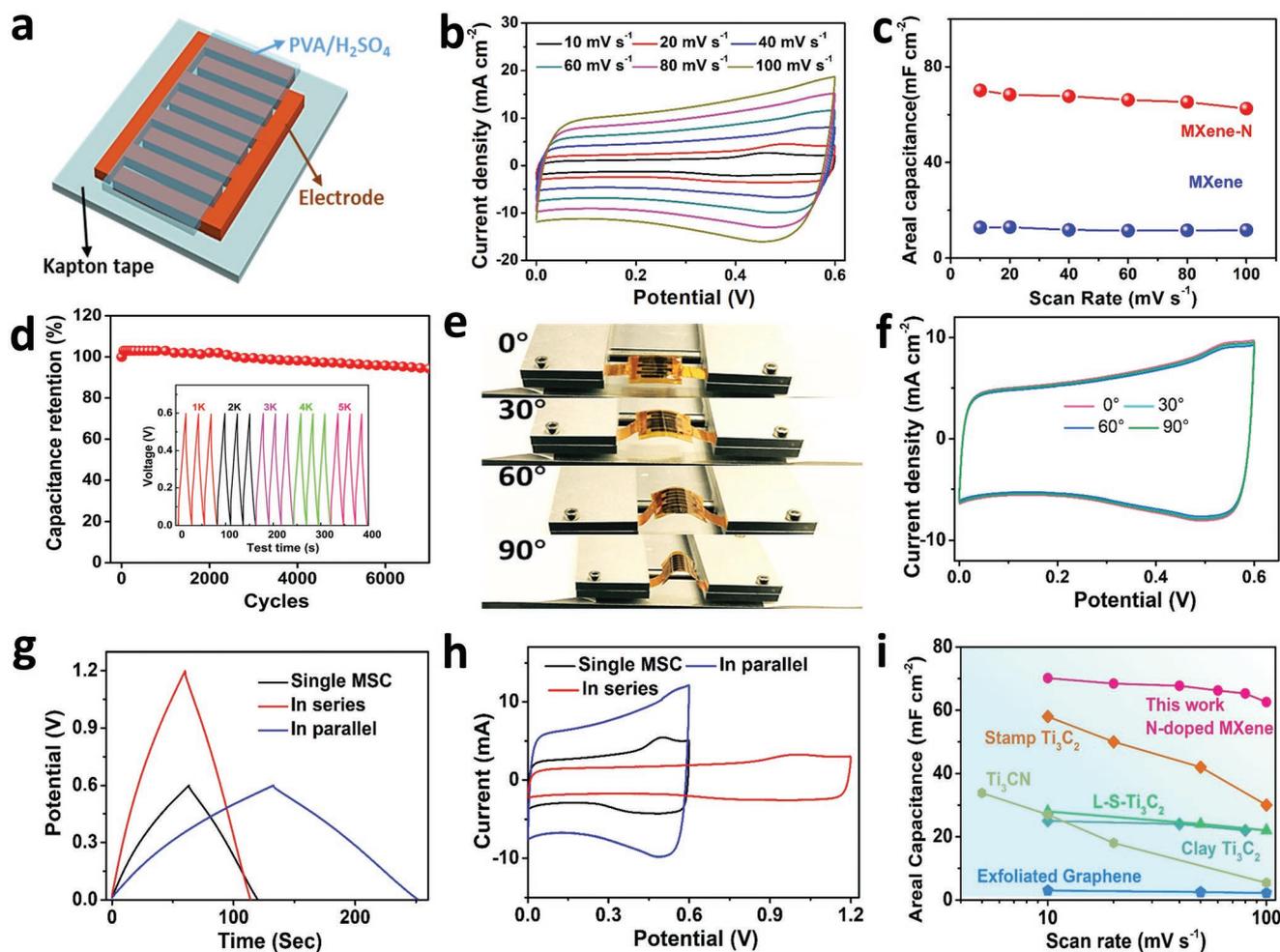
Figure 4. a) Schematics of a quasi-solid-state, all-MXene-N printed MSC device. b) CV profiles of all-MXene-N printed MSC at different scan rates of 10–100 mV s^{-1}. c) Comparison of the areal capacitances between MXene-N and MXene based MSCs. d) Cycle performance of all-MXene-N printed MSC. e) Photographs and f) CV profiles of all-MXene-N printed MSC under various bending angles 0°, 30°, 60°, and 90°. g) GCD profiles measured at 0.6 mA cm^{-2} and h) CV curves tested at 20 mV s^{-1} of two MXene-N based MSCs connected in series and in parallel. i) Comparison of the areal capacitances under different scan rates from recently published studies.

current densities, indicative of high reversibility of reactions (Figure S14, Supporting Information). In particular, Figure 4c draws a comparison of the areal capacitances between MXene-N and pristine MXene MSC devices. Benefiting from the 3D interconnected conductive networks, abundant nitrogen active sites, and free electrolyte transport channels, the crumpled MXene-N electrode exhibits superior charge storage behavior to that of pristine MXene counterpart. As such, MXene-N MSC device delivers favorable areal capacitances (70.1/62.5 mF cm^{-2} at 10/100 mV s^{-1}), which are markedly higher than those harvested by the pure MXene MSCs (13.8/11.1 mF cm^{-2} at 10/100 mV s^{-1}) (Figure S15, Supporting Information). Figure 4d presents the cyclic stability of MXene-N based quasi-solid-state MSC. Evidently, a 92% capacitance retention can be readily achieved after 7000 cycles at a current density of 5 mA cm^{-2}.

The device flexibility of MXene-N MSC was accordingly evaluated by CV tests under different bending conditions, as shown in Figure 4e. Upon the increase of the bending angle from 0° through 30° and 60° to 90°, there is no obvious change in the shapes of CV profiles (Figure 4f), demonstrating good mechanical robustness of thus-assembled MSC. Furthermore, to meet the capacitance and operating voltage requirements for practical applications, MSCs can be designed to be connected

in series and in parallel (Figure S16, Supporting Information). As revealed in the CV and GCD measurements (Figure 4g,h), the capacitance output can be easily doubled by two MSCs connecting in parallel; whilst double operating voltage output is attained upon connected in series. Figure 4i displays the performance comparison of areal capacitance of our work with recent studies on MXene (Ti$_3$C$_2$)-based quasi-solid-state MSCs. In this respect, our MXene-N MSC manifests advanced areal capacitance and rate capability as compared to the state-of-the-art systems, including Ti$_3$CN,[20] large-sized Ti$_3$C$_2$,[31] clay Ti$_3$C$_2$,[32] and exfoliated graphene.[33]

We further develop the 3D extrusion printing using viscous MXene-N based ink to fabricate high areal mass loading electrodes, demonstrating the versatility of MXene-N inks for printable energy storage applications. Such an ink was prepared by mixing crumpled MXene-N with AC, CNT, and GO to adjust the viscosity without using any insulating binders as additives (**Figure 5**a). At the same time, AC/CNT/GO ink was also prepared as the control. With the aid of 3D extrusion printing technique, various fine-printed patterns can be derived using prepared AC/CNT/MXene-N/GO ink, as shown in Figure 5b. For instance, printing a rigid "MXENE" scaffold with a height of ≈15 mm and freestanding woodpile architectures with programmable thickness. It is noted that the viscosity of the ink is key
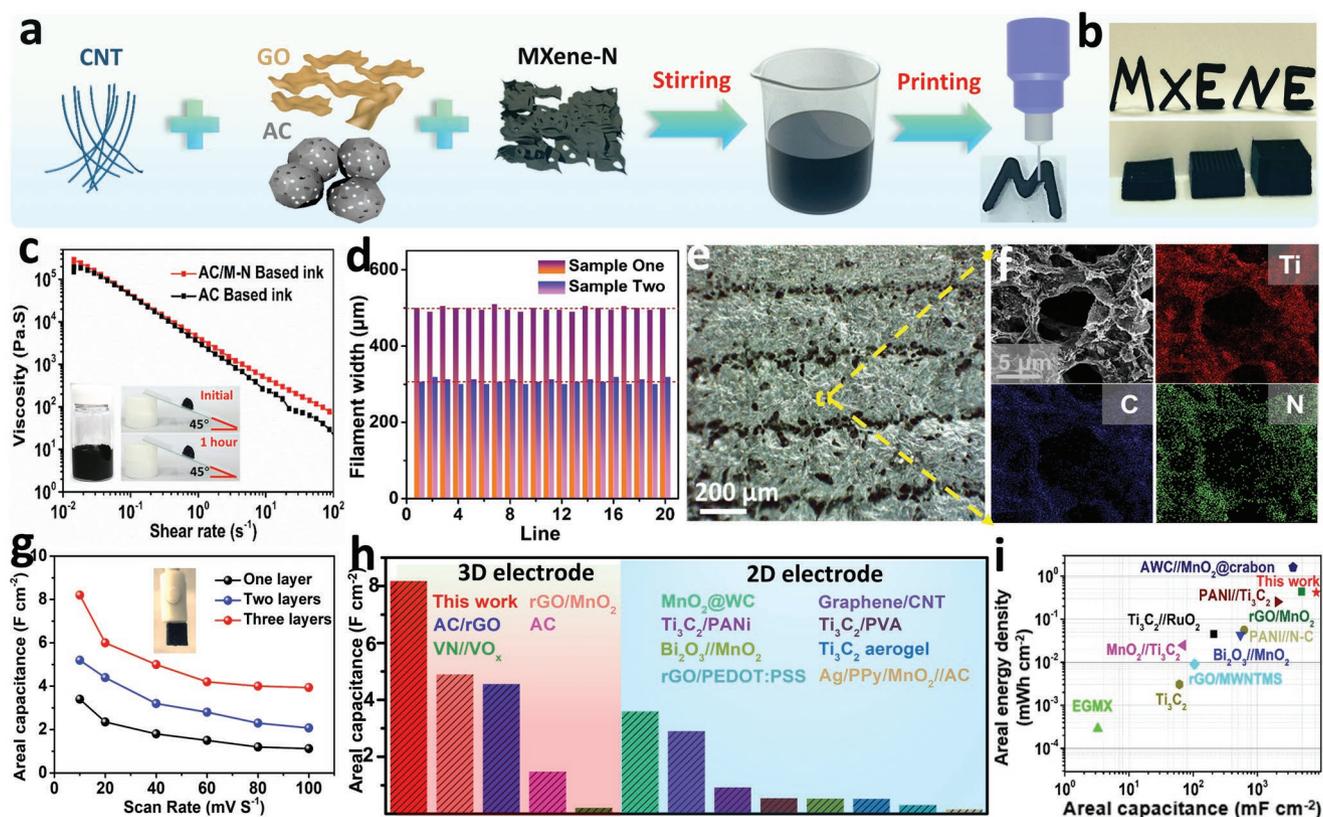
Figure 5. a) Schematic showing the preparation procedure of binder-free ink and 3D printing of designed patterns. b) Photographs showing the 3D-printed patterns by using the prepared AC/CNT/MXene-N/GO ink. c) Rheological behaviors of the AC/CNT/MXene-N/GO and AC/CNT/GO inks. d) The thickness of printing filament by applying two different nozzles. e,f) SEM image of the connected filament and corresponding elemental mapping. g) Relationship between printed layers and areal capacitances at different scan rates. h) Comparison of the areal capacitance of various electrodes at a scan rate of 10 mV s^{-1}. Left panel: Recently reported 3D electrodes. Right panel: 2D electrodes. i) Ragone plots of our 3D-printed SCs and other reported asymmetric/symmetric SCs.

to determining the 3D printing capability. To optimize the ink compositions for enabling 3D printing, rheological behaviors of AC/CNT/MXene-N/GO and AC/CNT/GO inks were studied (Figure 5c). Both inks manifest ideal shear thinning features, i.e., functioning as non-Newtonian fluids, which can avoid clogging during extrusion printing procedure. At a shear rate of 0.06 s^{-1}, both inks show a high viscosity (>10^4 Pa s). G' and G'' were also compared (Figure S17, Supporting Information) for both inks. The yield stress ($G' \geq G''$) is the transient point from the solid-state to liquid-like structure of the prepared inks.[34] As such, AC/CNT/MXene-N/GO and AC/CNT/GO inks exhibit a yield stress of 300 and 70 Pa, respectively. These rheological results suggest that the viscosity and yield stress are sufficient enough to realize good extrusion printing and stable 3D architectures (Figure 5c insets).[35] A literature survey on the yield stress of different ink materials and compositions used for extrusion printing is also conducted (Figure S18, Supporting Information). In addition, the effect of nozzle diameters onto the average width of the extrusion printed filaments was explored. Two different nozzles with a diameter of 190 and 260 µm were tested, resulting in the average width of 20 printed lines at ≈300 and 500 µm, respectively (Figure 5d). Under SEM inspection, the printed filament consists of uniformly interconnected structures (Figure 5e). In response, high-magnification SEM image and elemental mapping disclose the homogeneous distribution of Ti, C, and N elements within the porous frameworks (Figure 5f).

Electrochemical performance of 3D-printed electrodes was evaluated based on a three-electrode configuration using 3 M H$_2$SO$_4$ electrolyte. CV and GCD curves of MXene-N based electrode exhibit significantly larger area and enhanced pseudocapacitive contribution as compared to the control without MXene-N (Figures S19 and S20, Supporting Information). Electrochemical impedance spectroscopy tests further imply advanced electrode kinetics of MXene-N based electrode (Figure S21, Supporting Information). More interestingly, electrochemical measurements based on a symmetric two-electrode configuration were also enabled by employing MXene-N printed layers with different thicknesses (one, two, and three layers). Figure 5g summarizes the areal capacitance values measured for these layered electrodes, with corresponding CV profiles and GCD curves shown in Figure S22 in the Supporting Information. At a scan rate of 10 mV s^{-1}, all 3D-printed MXene-N based symmetric SCs manifest areal capacitance of 8.2, 5.2, and 3.4 F cm^{-2} for three-, two-, and one-layered electrode, respectively. In this respect, the 3D-printed electrode shows a superior areal capacitance value to those reported systems, including Ti$_3$C$_2$T$_x$, graphene, MnO$_2$, and AC based electrodes (Figure 5h).[2,14,15,36–43] Furthermore, the cycling performance of the 3D-printed MXene-N based symmetric SCs was further investigated. The capacitance retention remains 96.2% after 5000 cycles, indicating superior cycling stability (Figure S23, Supporting Information). The mass loadings and gravimetric capacitances of such symmetric SCs are further shown (Figure S24, Supporting Information). Even at a high current density of 12 mA cm^{-2}, the gravimetric capacitance of the 3D-printed SC with one-, two-, and three-layered electrode can still harvests 66.7, 55.6, and 45.1 F g^{-1}, respectively.

Meanwhile, benefiting from the high-mass-loading electrode architecture, our three-layered-electrode based SC readily harvests a high areal energy density of 0.42 mWh cm^{-2} at an areal capacitance of 8.2 F cm^{-2}, which compares favorably with the state-of-the-art printed SC systems such as activated wood carbon//MnO$_2$@carbon,[36] polyaniline (PANI)//Ti$_3$C$_2$,[43] PANI//N-C,[44] Bi$_2$O$_3$//MnO$_2$,[2] MnO$_2$//Ti$_3$C$_2$,[45] Ti$_3$C$_2$//RuO$_2$,[46] reduced graphene oxide (rGO)/multi-walled carbon nanotube microsphere,[47] Ti$_3$C$_2$,[20] Exfoliated graphene/MXene,[33] and rGO/MnO$_2$[14] (Figure 5i). Moreover, with the consideration of the compact electrode structure and crumpled morphology,[48] the three-layered-electrode device also attains a high volumetric energy density of 0.83 mWh cm^{-3}, superior to those of recently reported SC systems (Figure S25, Supporting Information).

3. Conclusions

In summary, we have demonstrated the design of two types of MXene-N based inks with different viscosity toward the construction of printable electrochemical energy storage devices. Pure MXene-N ink with a relatively low viscosity is feasible to fabricate interdigitated MSCs with the aid of 2D screen printing technique, readily harvesting a favorable areal capacitance of 70.1 mF cm^{-2}. Moreover, highly viscous, binder-free MXene-N based ink is versatile enough to construct 3D-printed SC devices with controllable electrode thickness by extrusion printing. As a result, the derived symmetric supercapacitor exhibits a high areal and volumetric energy density of 0.42 mWh cm^{-2} and 0.83 mWh cm^{-3}, respectively. This work offers a rational solution to print multidimensional electrode architectures for building up high-energy-density electrochemical energy storage systems.

Supporting Information

Supporting Information is available from the Wiley Online Library or from the author.

Conflict of Interest

The authors declare no conflict of interest.

ADVANCED
SCIENCE NEWS
www.advancedsciencenews.com

ADVANCED
ENERGY
MATERIALS
www.advenergymat.de

[1] C. F. Zhang, L. McKeon, M. P. Kremer, S. H. Park, O. Ronan, A. Seral-Ascaso, S. Barwich, C. O. Coileain, N. McEvoy, H. C. Nerl, B. Anasori, J. N. Coleman, Y. Gogotsi, V. Nicolosi, *Nat. Commun.* **2019**, *10*, 1795.

[2] H. Xu, X. Hu, H. Yang, Y. Sun, C. Hu, Y. Huang, *Adv. Energy Mater.* **2015**, *5*, 1401882.

[3] F Zhou, C. H. Xiao, S. H. Zheng, X. Y. Shi, J. Q. Qin, Q. Fu, X. H. Bao, X. L. Feng, K Müllen, Z. S. Wu, *J. Am. Chem. Soc.* **2018**, *140*, 8198.

[4] M. Boota, Y. Gogotsi, *Adv. Energy Mater.* **2019**, *9*, 1802917.

[5] L. Feng, K. Wang, X. Zhang, X. Sun, C. Li, X. Ge, Y. Ma, *Adv. Funct. Mater.* **2018**, *28*, 1704463.

[6] Y. Y. Yi, L. H. Yu, Z. N. Tian, Y. Z. Song, Y. L. Shao, L. J. Gao, J. Y. Sun, Z. F. Liu, *Adv. Funct. Mater.* **2018**, *28*, 1805510.

[7] L. H. Yu, Y. Y. Yi, T. Yao, Y. Song, Y. Chen, Q. Li, Z. Xia, N. Wei, Z. N. Tian, B. Nie, L. Zhang, Z. F. Liu, J. Y. Sun, *Nano Res.* **2019**, *12*, 331.

[8] Y. Lin, Y. Gao, F. Fang, Z. Fan, *Nano Res.* **2018**, *11*, 3065.

[9] S. Zheng, J. Ma, Z. S. Wu, F. Zhou, Y. B. He, F. Kang, H. M. Cheng, X. H. Bao, *Energy Environ. Sci.* **2018**, *11*, 2001.

[10] Y. L. Shao, J. Li, Y. Li, H. Wang, Q. Zhang, R. B. Kaner, *Mater. Horiz.* **2017**, *4*, 1145.

[11] Y. F. Xu, M. G. Schwab, A. J. Strudwick, I. Hennig, X. L. Feng, Z. S. Wu, K. Müllen, *Adv. Energy Mater.* **2013**, *3*, 1035.

[12] X. Tang, H. Zhou, Z. Cai, D. Cheng, P. He, P. Xie, D. Zhang, T. Fan, *ACS Nano* **2018**, *12*, 3502.

[13] J. Zhao, Y. Zhang, X. Zhao, R. Wang, J. Xie, C. Yang, J. Wang, Q. Zhang, L. Li, C. Lu, Y. Yao, *Adv. Funct. Mater.* **2019**, *29*, 1900809.

[14] B. Yao, S. Chandrasekaran, J. Zhang, W. Xiao, F. Qian, C. Zhu, E. B. Duoss, C. M. Spadaccini, M. A. Worsley, Y. Li, *Joule* **2019**, *3*, 459.

[15] K. Shen, J. Ding, S. Yang, *Adv. Energy Mater.* **2018**, *8*, 1800408.

[16] T. Liu, L. Zhang, W. You, J. Yu, *Small* **2018**, *14*, 1702407.

[17] Y. Q. Jiang, Z. Xu, T. Q. Huang, Y. J. Liu, F. Guo, J. B. Xi, W. W Gao, C. Gao, *Adv. Funct. Mater.* **2018**, *28*, 1707024.

[18] L. Y. Yu, B. Anasori, Y. T. Liu, Q. Z. Zhu, P Zhang, Y. Gogotsi, B. Xu, *ACS Energy Lett.* **2018**, *3*, 1597.

[19] B. Chen, Y. Jiang, X. Tang, Y. Pan, S. Hu, *ACS Appl. Mater. Interfaces* **2017**, *9*, 28433.

[20] C. F. Zhang, M. P. Kremer, A. Ascaso, S. Park, N. McEvoy, B. A. Niall, Y. Gogotsi, V. Nicolosi, *Adv. Funct. Mater.* **2018**, *28*, 1705506.

[21] J. Zhang, S. Seyedin, S. Qin, Z. Wang, S. Moradi, F. Yang, P. A. Lynch, W. Yang, J. Liu, X. Wang, J. M. Razal, *Small* **2019**, *15*, 1804732.

[22] A. K. Thakur, M. Majumder, R. B. Choudhary, S. B. Singh, *J. Power Sources* **2018**, *402*, 163.

[23] W. Z. Bao, L. Liu, C. Y. Wang, S. Choi, D. Wang, G. X. Wang, *Adv. Energy Mater.* **2018**, *8*, 1702485.

[24] W. W. Zhao, J. L. Peng, W. K. Wang, B. B. Jin, T. T Chen, S. J. Liu, Q. Zhao, W. Huang, *Small* **2019**, *15*, 1901351.

[25] M. Q. Zhao, X. Q. Xie, C. Ren, T. Makaryan, B. Anasori, G. X. Wang, Y. Gogotsi, *Adv. Mater.* **2017**, *29*, 1702410.

[26] Z. M. Fan, Y. S. Wang, Z. M. Xie, D. L. Wang, Y. Yuan, H. J. Kang, B. L. Su, Z. J. Cheng, Y. Y. Liu, *Adv. Sci.* **2018**, *5*, 1800750.

[27] K. Ma, H. Jiang, Y. J. Hu, C. Z. Li, *Adv. Funct. Mater.* **2018**, *28*, 1804306.

[28] C. H. Yang, Y. Tang, Y. P. Tian, Y. Y. Luo, M. F. Ud Din, X. T. Yin, W. X. Que, *Adv. Energy Mater.* **2018**, *8*, 1802087.

[29] Y. Y. Wen, T. E. Rufford, X. Z. Chen, N. Li, M. Q. Lyu, L. M. Dai, L. Z. Wang, *Nano Energy* **2017**, *38*, 368.

[30] W. Z. Bao, X. Tang, X. Guo, S. Choi, C. Y. Wang, Y. Gogotsi, G. X. Wang, *Joule* **2018**, *2*, 778.

[31] Y. Y. Peng, B. Akuzum, N. Kurra, M. Q. Zhao, M. Alhabeb, B. Anasori, E. C. Kumbur, H. N. Alshareef, M. D. Ger, Y. Gogotsi, *Energy Environ. Sci.* **2016**, *9*, 2847.

[32] H. Wang, Y. Wu, X. Yuan, G. Zeng, J. Zhou, X. Wang, J. W. Chew, *Adv. Mater.* **2018**, *30*, 1704561.

[33] H. Li, Y. Hou, F. Wang, M. R. Lohe, X. Zhuang, L. Niu, X. Feng, *Adv. Energy Mater.* **2017**, *7*, 1601847.

[34] F. Zhang, M. Wei, V. V. Viswanathan, B. Swart, Y. Shao, G. Wu, C. Zhou, *Nano Energy* **2017**, *40*, 418.

[35] W. B. Li, Y. H. Li, M. Su, B. X. An, J. Liu, D. Su, L. Li, F. Y. Li, Y. L. Song, *J. Mater. Chem. A* **2017**, *5*, 16281.

[36] C. J. Chen, Y. Zhang, Y. J. Li, J. Q. Dai, J. W. Song, Y. G. Yao, Y. H. Gong, I. Kierzewski, J. Xie, L. B. Hu, *Energy Environ. Sci.* **2017**, *10*, 538.

[37] B. S. Kim, K. Lee, S. Kang, S. Lee, J. B. Pyo, I. S. Choi, K. Char, J. H. Park, S. S. Lee, J. Lee, J. G. Son, *Nanoscale* **2017**, *9*, 13272.

[38] L. Liu, Q. Tian, W. Yao, M. Li, Y. Li, W. Wu, *J. Power Sources* **2018**, *397*, 59.

[39] T. T. Gao, Z. Zhou, J. Y. Yu, J. Zhao, G. L. Wang, D. X. Cao, B. Ding, Y. J. Li, *Adv. Energy Mater.* **2019**, *9*, 1802578.

[40] M. Areir, Y. M. Xu, D. Harrison, J. Fyson, *Mater. Sci. Eng., B* **2017**, *226*, 29.

[41] G. X. Qu, J. L. Cheng, X. D. Li, D. M. Yuan, P. N. Chen, X. L. Chen, B. Wang, H. S. Peng, *Adv. Mater.* **2016**, *28*, 3646.

[42] Z. Ling, C. E. Ren, M. Q. Zhao, J. Yang, J. M. Giammarco, J. S. Qiu, M. W. Barsouma, Y. Gogotsi, *Proc. Natl. Acad. Sci. USA* **2014**, *111*, 16676.

[43] Y. M. Wang, X. Wang, X. L. Li, Y. Bai, H. H. Xiao, Y. Liu, R Liu, G. H. Yuan, *Adv. Funct. Mater.* **2019**, *29*, 1900326.

[44] J. Cao, T. Huang, R. L. Liu, X. Xi, D. Q. Wu, *Electrochim. Acta* **2017**, *230*, 265.

[45] J. Zhou, J. Yu, L. Shi, Z. Wang, H. Liu, B. Yang, C. Li, C. Zhu, J. Xu, *Small* **2018**, *14*, 1803786.

[46] Q. Jiang, N. Kurra, M. Alhabeb, Y. Gogotsi, H. N. Alshareef, *Adv. Energy Mater.* **2018**, *8*, 1703043.

[47] S. Gao, K. Wang, Z. Du, Y. Wang, A. Yuan, W. Lu, L. W. Chen, *Carbon* **2015**, *92*, 254.

[48] J. Zhao, Y. Zhang, Y. Huang, X. Zhao, Y. Shi, J. Qu, C. Yang, J. Xie, J. Wang, L. Li, Q. Yan, S. Hou, C. Lu, X. Xu, Y. Yao, *J. Mater. Chem. A* **2019**, *7*, 972.